arXiv:1608.05643v1 [cond-mat.mes-hall] 19 Aug 2016

Monitoring Electrostatically-Induced Deflection, Strain and Doping in Suspended Graphene using Raman Spectroscopy

Dominik Metten, Guillaume Froehlicher, and Stéphane Berciaud*
Institut de Physique et Chimie des Matériaux de Strasbourg and NIE, UMR 7504, Université de Strasbourg and CNRS, 23 rue du Læss, BP43, 67034 Strasbourg Cedex 2, France

Electrostatic gating offers elegant ways to simultaneously strain and dope atomically thin membranes. Here, we report on a detailed *in situ* Raman scattering study on graphene, suspended over a Si/SiO_2 substrate. In such a layered structure, the intensity of the Raman G- and 2D-mode features of graphene are strongly modulated by optical interference effects and allow an accurate determination of the electrostatically-induced membrane deflection, up to irreversible collapse. The membrane deflection is successfully described by an electromechanical model, which we also use to provide useful guidelines for device engineering. In addition, electrostatically-induced tensile strain is determined by examining the softening of the Raman features. Due to a small residual charge inhomogeneity $\sim 5 \times 10^{10}$ cm^{-2}, we find that non-adiabatic anomalous phonon softening is negligible compared to strain-induced phonon softening. These results open perspectives for innovative Raman scattering-based readout schemes in two-dimensional nanoresonators.

Keywords: suspended graphene, two-dimensional materials, Raman spectroscopy, strain, doping, optical interference, NEMS.

Introduction Electrostatic gating is one of the most commonly employed actuation schemes in nanomechanical resonators [1]. In particular, field-effect transistor geometries have been adapted to fabricate nanoelectromechanical resonators using individual carbon nanotubes [2], graphene [3, 4] and, more recently, atomically thin transition metal dichalcogenides [5, 6]. In such devices, the ultimate thinness of the suspended nanoresonator leads to high electromechanical susceptibility and possible coupling between electrostatically-induced strain and doping. As a classic example, similar designs of suspended graphene transistors have been used not only to fabricate electro-mechanical [4] or opto-electromechanical devices [3, 7, 8] but also to probe quasi-ballistic electron transport [9, 10] and many-body effects [11, 12] in the vicinity of graphene's charge neutrality (Dirac) point. Electrostatic pressure can thus intentionally be applied to control the position, shape, and motion of an atomically thin suspended membrane but may also be an undesired side-effect when examining intrinsic transport properties [13–15], ultimately leading to irreversible collapse [9, 16]. As a result, *in situ* probes are needed in order to examine the subtle interplay between doping, electron transport, motion and strain in electrostatically-actuated membranes.

Here, we employ micro-Raman scattering spectroscopy as a minimally invasive and highly accurate technique to simultaneously monitor electrostatically-induced deflection, strain and doping in a pristine suspended graphene monolayer. Our analysis is based on the large changes in intensity, frequency, and linewidth of the main Raman features of graphene subjected to an electrostatic pressure. The measured deflection is well-captured by an electromechanical model [15–17], which solely uses the built-in tension in graphene as a fitting parameter. Our model accurately predicts the critical gate bias and highest doping level achievable before device collapse, therefore providing useful guidelines for opto-electromechanical device engineering. Here, the charge carrier density remains significantly below 10^{12} cm^{-2}, with a small residual charge inhomogeneity of $\sim 5 \times 10^{10}$ cm^{-2}. In these conditions, the Raman features of electrostatically-gated suspended graphene are chiefly affected by strain-induced phonon softening, with only minor contributions from non-adiabatic electron-phonon coupling [18–20].

Methods Our typical sample consists of a mechanically exfoliated graphene monolayer suspended over a 4.9 μm-wide trench pre-patterned by optical lithography and reactive ion etching on a Si/SiO_2 substrate (oxide thickness of 500 nm, of which $h_{SiO_2} = 212 \pm 5$ nm of SiO_2 are left) [23]. The suspended monolayers (1LG) are identified via optical microscopy and Raman spectroscopy as discussed below. To avoid contamination with resist and solvents, Ti/Au contacts are evaporated through a transmission electron microscopy grid, used as a shadow mask (see Fig. 1a,b). Finally, the gold contact pads are wire-bonded and the sample is cooled down to 4 K using an He flow optical cryostat. Micro-Raman spectra are recorded as a function of the back-gate voltage V_g in back-scattering geometry using a laser beam with a wavelength of 532 nm focused onto a $\approx$ 1.2μm-diameter spot onto the sample using a 50$\times$ objective with a numerical aperture of 0.65. The laser power impinging on the sample is maintained below 300 μW to avoid photothermally-induced changes in the Raman features and sample damage. In the following, we focus on the Raman G and 2D modes, which involve zone-center and near zone-edge optical phonons, respectively [24]. The defect-allowed D-mode has a negligible intensity and is not considered here.

* stephane.berciaud@ipcms.unistra.fr

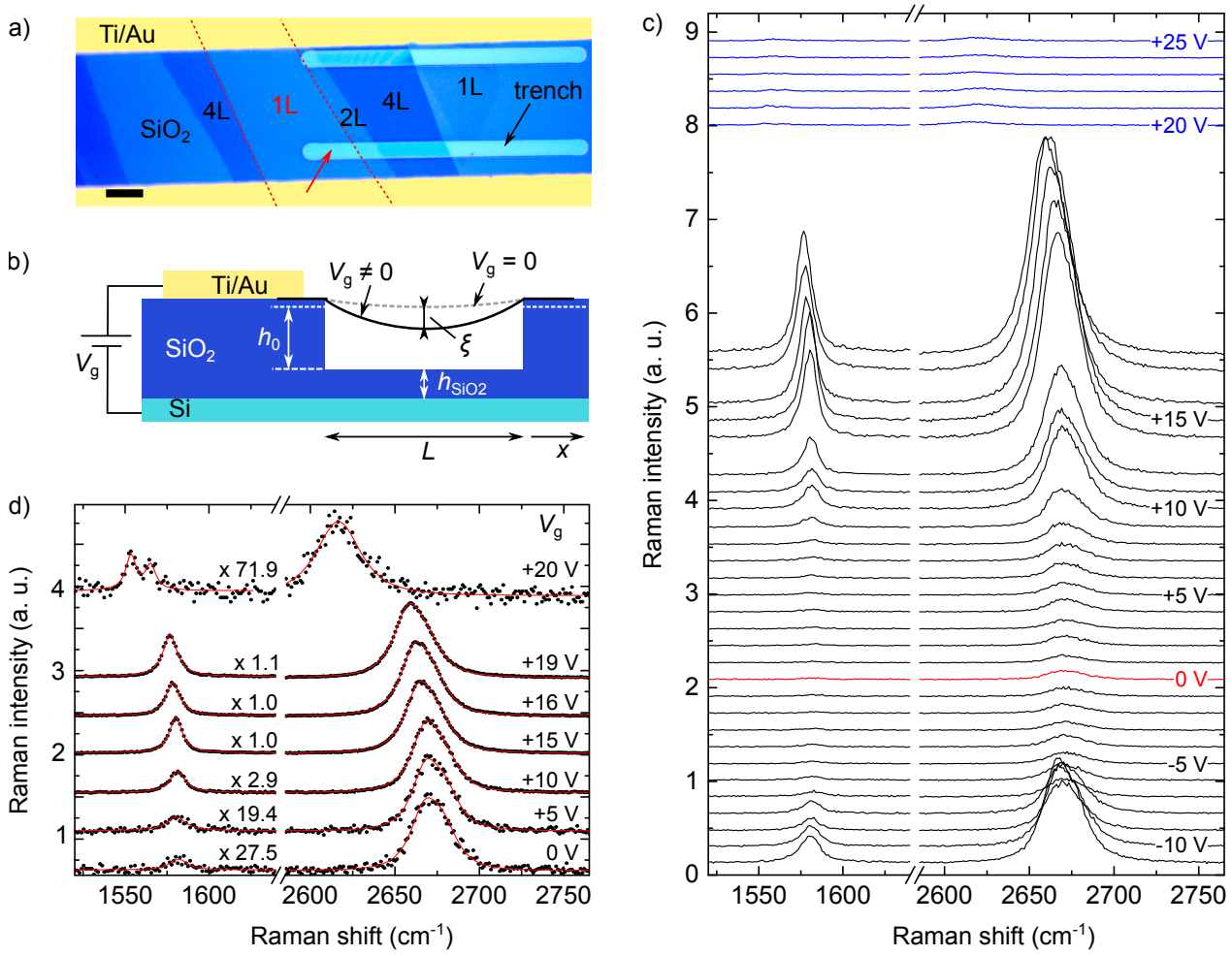

FIG. 1. (a) Optical micrograph of a suspended graphene device. The red dashed line marks the limit of the graphene monolayer (1L), which is neighbored by a bi- and tetralayer. The scale bar is 10 μm. (b) Schematic side view of the device. (c) Cascade plot of Raman spectra recorded in the middle of the suspended graphene membrane, as a function of V_g. Spectra are recorded at 4 K. The spectrum at $V_g = 0$ is drawn in red. Spectra recorded after sample collapse ($V_g > +19$ V) are shown in blue. (d) Selected Raman spectra for different V_g, normalized with respect to the integrated intensity of the 2D-mode feature. The red solid lines are fits to the G- (2D-) mode features using Lorentzian (modified Lorentzian [21, 22]) profiles.

The peak frequency ω_G (ω_{2D}), full-width at half maximum Γ_G (Γ_{2D}), and integrated intensity I_G (I_{2D}) of the G-mode and 2D-mode features are extracted from single Lorentzian and modified Lorentzian fits [21, 22], respectively. As previously demonstrated [9–11, 22, 23, 25, 26] and also shown in the Supporting Information, suspended graphene exhibits low residual charge carrier density and inhomogeneity, both below 10^{11} cm^{-2}. Consequently, we assume that graphene is quasi neutral at $V_g = 0$ V. We note h_0, the initial distance between the membrane and the underlying SiO_2 layer at $V_g = 0$ and ξ the gate-induced deflection in the middle of the trench (see Fig. 1b).

Electrostatically-induced deflection Figure 1c shows a cascade plot of Raman spectra recorded during a gate bias sweep from $V_g = -11$ V to $V_g = +25$ V. Several interesting features can be observed as V_g rises up to +19 V. First, the integrated intensity of the Raman features increases strikingly. Second, as can be more clearly seen in Fig. 1d, the integrated intensity ratio of the 2D- and G-mode features, I_{2D}/I_G, augments significantly. Third, the Raman G- and 2D-mode features downshift. The first and second observations stem from optical interference effects, which have a drastic impact on the Raman intensities in graphene devices within a multilayered structure [27–29]. Indeed, the applied gate bias induces an electrostatic pressure that pulls the graphene layer towards the underlying SiO_2 layer, leading to gate-dependent Raman enhancement factors. For a quantitative analysis, I_G and I_{2D} are plotted as a function of V_g in Fig. 2a (this plot includes a gate sweep from $V_g = 0$ to -12 V and from -12 to +25 V), along with,

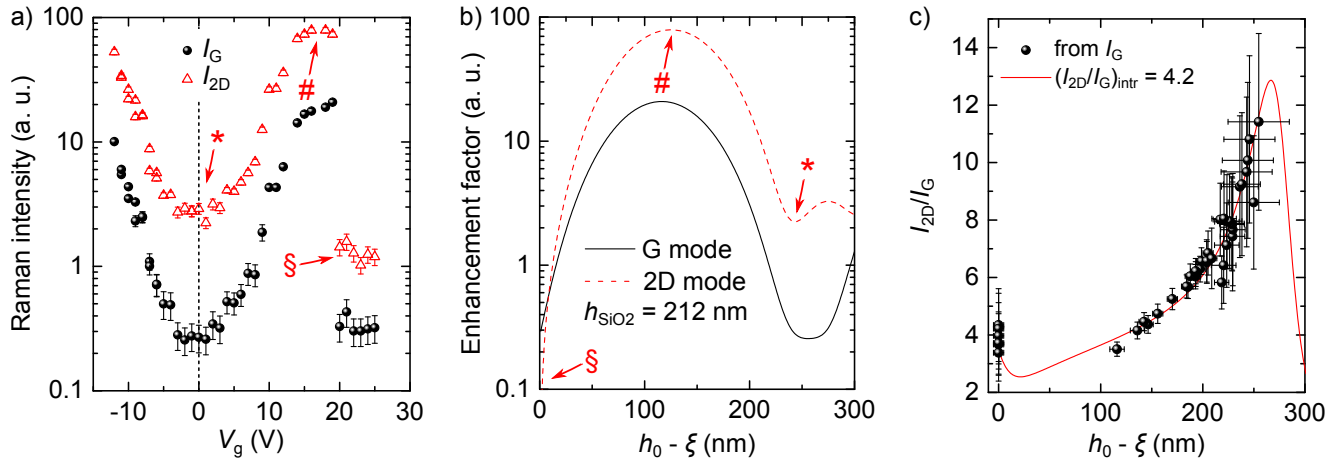

FIG. 2. (a) Semilogarithmic plot of I_G (filled black squares) and I_{2D} (open red triangles) as a function of V_g. (b) Raman enhancement factors as a function of $h_0 - \xi$, the distance between graphene and the SiO_2 layer, calculated for $h_{SiO_2} = 212\,\text{nm}$ and $\lambda_{laser} = 532\,\text{nm}$. The calculated Raman intensities at heights marked with star, hash and paragraph symbols in (b) can be identified in (a). (c) Evolution of I_{2D}/I_G as a function of $h_0 - \xi$, determined from the evolution of I_G with V_g. The red line is a fit based on a multiple interference model using an *interference-free* reference value of $(I_{2D}/I_G)_{intr} = 4.2$.

in Fig. 2b, the Raman enhancement factors for the G- and 2D-mode features, computed using a multiple interference model [27, 29]. From this model, we are able to estimate the central deflection ξ.

Here, I_G and I_{2D} are minimal for $V_g = 0$ and, as expected, show nearly identical behaviors at positive and negative V_g. Interestingly, I_{2D} increases from its minimal value at $V_g \approx 0$ to a maximum at $V_g = +17\,\text{V}$, which we assign to an initial height $h_0 \approx 250 \pm 20$ nm and to a deflection $\xi = 134 \pm 5$ nm, respectively. We note that h_0 is a little smaller than the actual depth of the trench (288 ± 5 nm), implying that the graphene membrane is slightly concave. This situation may be attributed to the mismatch between the thermal expansion coefficients of the Si/SiO_2 substrate and of graphene [30, 31], as well as to the native slack of the as-exfoliated sample and adhesion to the sidewalls of the trench [4, 29, 32–34]. Since the Raman-scattered G- and 2D-mode photons have different wavelengths, the measured ratio I_{2D}/I_G, also depends on ξ (see Fig. 2c) [27, 35] and is in very good agreement with the calculated Raman enhancement factors [36] using an interference-free intrinsic ratio $(I_{2D}/I_G)_{intr}$ of 4.2 ± 0.5, consistent with our previous findings [35].

The sudden drop in the Raman intensities above $V_g = +19\,\text{V}$ (see Fig. 1c-d and 2a) is inconsistent with a continuous increase of ξ and is a strong indication that the membrane has collapsed and now adheres strongly to the underlying SiO_2 layer. Indeed, the Raman intensity is expected to be very low for the layered system $Si/SiO_2(212\,\text{nm})$/graphene/vacuum when $\xi \to h_0$ (see Fig. 2b). The drop in the Raman intensities is accompanied by a downshift of the G- and 2D-mode features and by a splitting of the G-mode feature, characteristic of sizable uniaxial strain [37, 38] (see Fig. 1d). These observations suggest that the membrane remains attached on the edges of the trench, as confirmed by scanning electron microscopy (SEM) imaging (see Supporting Information). The G- and 2D-mode downshifts allow us to estimate a uniaxial strain of $\sim 1\%$ [37], that is consistent with a rough estimation based on the SEM image.

Fig. 3a displays ξ as a function of V_g, extracted from the variations of I_G. Very similar results are obtained from the analysis of I_{2D} (see Supporting Information). The large error bars near $V_g = 0$ account for the broad valley in the interference pattern (see Fig. 2b). From the theory of elasticity [15, 16], ξ is connected to a (here electrostatic) pressure load p_{el} through

$$p_{el}(\xi) = \frac{64Et}{3(1-\nu^2)L^4}\,\xi^3 + \frac{8T_0}{L^2}\,\xi, \qquad (1)$$

where E is the Young's modulus, ν the Poisson ratio, t the thickness of the membrane, T_0 its built-in tension, and L the trench width (see Fig. 1b). The scaling $p_{el} \propto \xi^3$ is well-known for membranes (with no bending rigidity) [39–41], and T_0 can be interpreted as an effective bending rigidity moderating the deflection, as p_{el} scales linearly with ξ for thin plates [15, 17, 42–44]. Eq. (1) is obtained by assuming translational invariance along the trench and a parabolic membrane profile perpendicular to the trench (x direction), which is a first approximation, because back-coupling mechanisms between deflection and charge redistribution may affect the membrane profile [15]. Noteworthy, Eq. (1) also involves a uniform pressure load over the membrane, which is not the case in our experiment since ξ attains values that are on the same order of magnitude as h_0. However, we can model our experimental data by considering an effective value of p_{el}, obtained by averaging the local capacitance $c(x)$

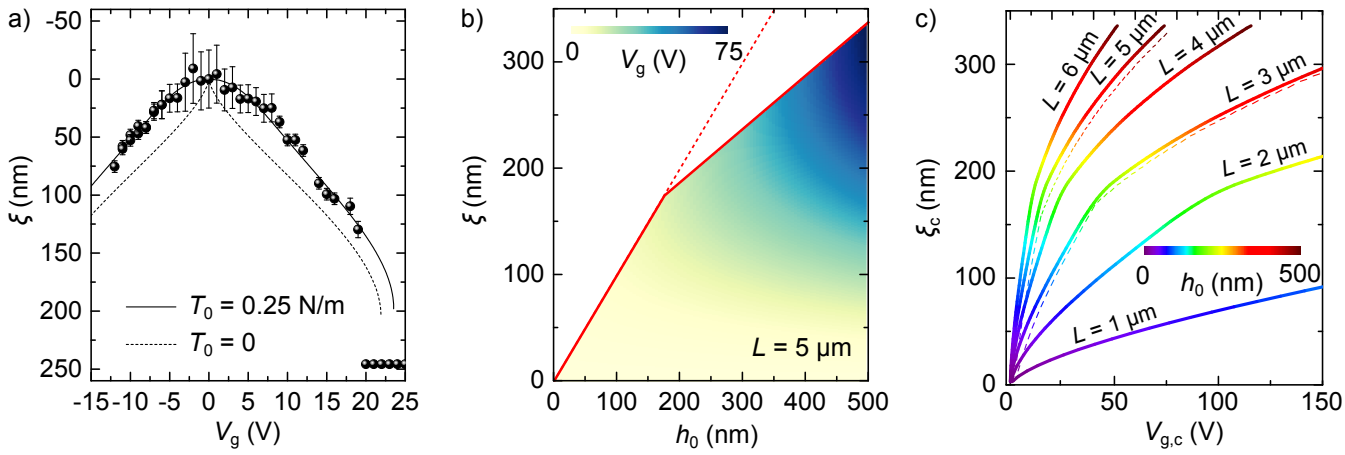

FIG. 3. (a) Graphene deflection ξ in the middle of the trench, determined from the variation of I_G, as a function of V_g. The dashed (solid) line is a fit obtained by solving Eq. (1) with $T_0 = 0$ ($T_0 = 0.25\,$N/m). (b) False color map of the gate voltage required to attain a given ξ as a function of h_0, for $L = 5\,\mu$m and an initial SiO_2 thickness of 500 nm (see Fig. 1b). (c) Critical deflection ξ_c as a function of the corresponding critical gate voltage $V_{g,c}$. The data are extracted from color plots, as in (b), by going along the border highlighted with a solid red line in (b). The critical (straight) lines are shown for different trench widths L. The color code indicates the corresponding h_0. For $L = 3$ and $5\,\mu$m, the critical (dashed) lines are added for a finite $T_0 = 0.3$ N/m.

along the parabolic profile (see Fig. 1b) [16]:

$$p_{el}(\xi) = \frac{V_g^2}{2\varepsilon_0} \int_{-L/2}^{+L/2} c^2(x)\ \frac{dx}{L}, \qquad (2)$$

with $c(x) = (c_0^{-1}(x) + c_{SiO_2}^{-1})^{-1}$, $c_{SiO_2} = \varepsilon_0\varepsilon_{SiO_2}/(h_{SiO_2})$ and $c_0(x) = \varepsilon_0/(h(x))$, where $h(x)$ is the distance between the SiO_2 layer and the membrane, ε_0 is the vacuum permittivity and $\epsilon_{SiO_2} \approx 3.9$ is the DC dielectric constant of SiO_2. We can thus compute ξ as a function of V_g by injecting Eq. (2) into Eq. (1) and solving the resulting equation numerically.

As shown in Fig. 3a, our experimental measurements of ξ vs V_g are very well fit to Eq. (1), using $E = 1.05\,$TPa, $t = 0.335\,$nm and $\nu = 0.16$ [29, 45–47] and leaving $T_0 = 0.25 \pm 0.03\,$N/m as the only fitting parameter. This value corresponds to a built-in tension of $0.07 \pm 0.01\%$, which is consistent with previous studies of suspended graphene monolayers [3, 4, 13, 26, 46]. Let us note that the good agreement between our data and our model using an *intrinsic* value of E [16, 29, 46–48] suggests that crumpling in our mechanically exfoliated graphene membrane can presumably be neglected [49].

Interestingly, Eq. (1) has no real solution above a critical gate voltage $V_{g,c}$. In particular, our model predicts an abrupt increase of ξ for $V_g > +20\,$V up to $+23.5\,$V, consistent with the collapse of the membrane observed for $V_g > +19$ V. We rely on the good accordance of our data with the electromechanical model to calculate the gate-induced deflection for a range of h_0 and compute the critical voltage $V_{g,c}$ above which no real solution is found. The resulting contour plot is shown in Fig. 3b for $L = 5\ \mu$m and an initial SiO_2 thickess of 500 nm. Interestingly, for $h_0 < 180$ nm, we find that increasing V_g leads to a smooth deposition of the graphene layer onto the underlying SiO_2 substrate (*i.e.,* the critical deflection $\xi_c = h_0$), whereas for $h_0 > 180$ nm (as is the case in our experiment) the membrane abruptly collapses after reaching a value $\xi_c < h_0$. Now, another interesting question for device optimization is, which voltage does a membrane sustain (oxide breakdown notwithstanding) until the membrane collapses? In Fig. 3c, the critical lines (ξ_c *vs* $V_{g,c}$) are shown for different L, with color-coded h_0. In order to estimate the impact of a typical built-in tension, the critical lines for $L = 3$ and $5\,\mu$m are added for $T_0 = 0.3\,$N/m. A finite built-in tension slightly shifts the curves to higher $V_{g,c}$ and retards the deflection and the collapse. Similar simulations for trenches etched in a Si/SiO_2 substrate with initial SiO_2 thicknesses of 285 nm and 90 nm are reported in the Supporting Information.

Electrostatically-induced strain and doping The strength of our Raman scattering-based study lies not only in the *in situ* determination of the membrane deflection, but also in the possibility of simultaneously extract local information about strain and doping, which is encoded in the Raman frequencies and linewidths. In Fig. 4a, we show the evolution of ω_G and ω_{2D} with V_g, extracted from the spectra in Fig. 1c. The maximum Raman frequencies at $V_g = 0$ are $1582.6\,cm^{-1}$ and $2669.4\,cm^{-1}$, respectively. Both frequencies downshift with increasing V_g and a linear correlation is observed between ω_{2D} and ω_G, with a slope of 2.0 ± 0.2 similar to previously observed values in strained graphene [26, 29, 37, 38, 53–55] (see Fig. 4b). However,

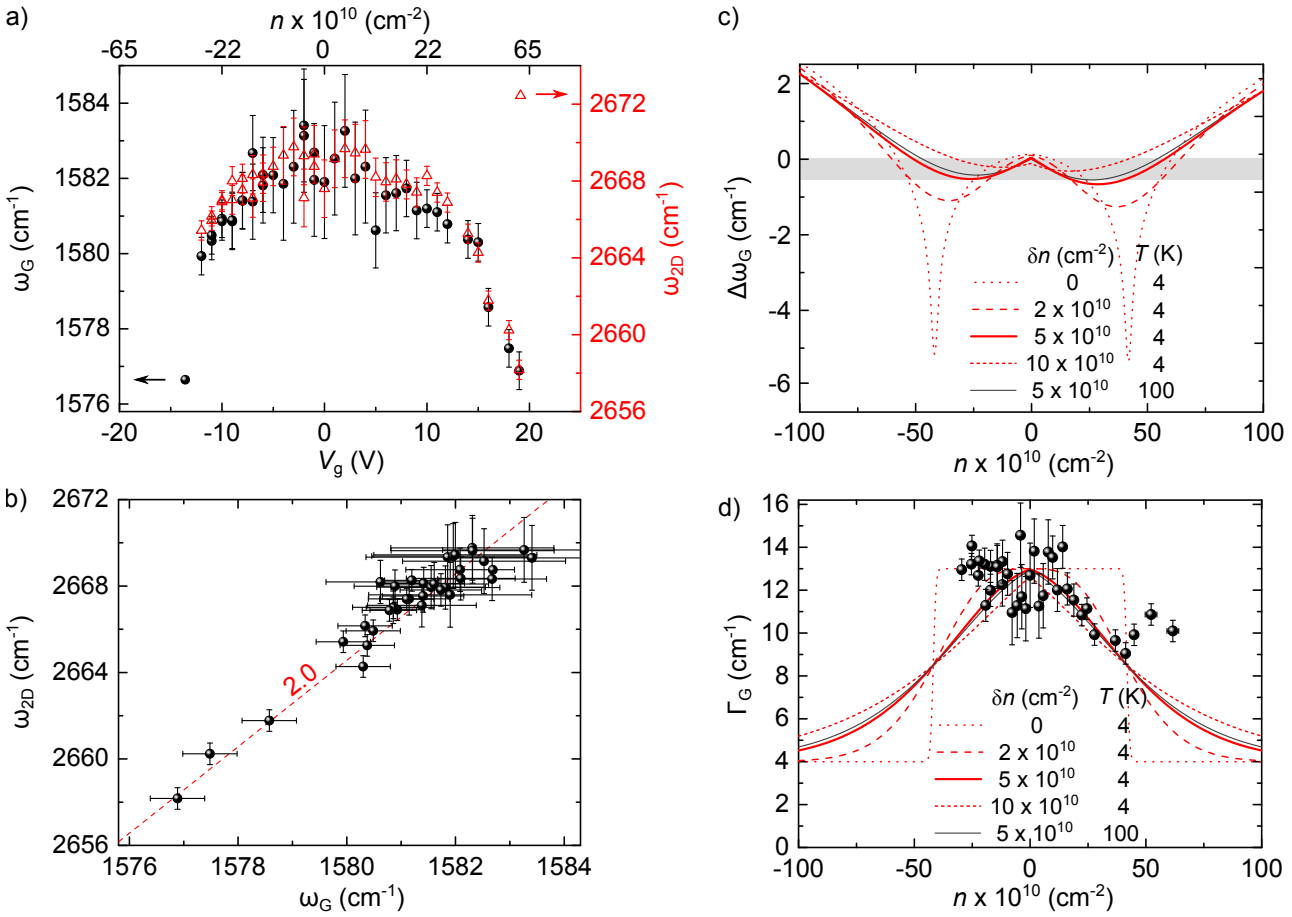

FIG. 4. (a) ω_G (black spheres) and ω_{2D} (red triangles) as a function of V_g. (b) Correlation between ω_{2D} and ω_G. The red line is a linear curve with a slope of 2.0. (c) Theoretically predicted shift of the Raman G-mode frequency ($\Delta\omega_G$) and (d) full width at half maximum Γ_G due to electron-phonon coupling, calculated as in Refs. [18, 50]. Calculations are performed as a function of the charge carrier density n for T = 4 K (red lines) and T = 100 K (thin gray line), using a Fermi velocity of 1.3×10^6 m/s [11, 12], an electron-phonon coupling constant of 3.6×10^{-3}, and considering various levels of residual charge inhomogeneity δn, as in Ref. [51]. Our experimental measurements of Γ_G (black symbols) are compared to calculations in (d). The gray bar in (c) illustrates the very small G-mode frequency shifts due to electron-phonon coupling predicted for a realistic value of $\delta n = 5 \times 10^{10}$ cm^{-2}. A residual contribution of 4 cm^{-1} due to our spectral resolution and phonon anharmonicities [52] is added to Γ_G in (d).

the gate bias also dopes graphene. A $T = 4$ K, as the Fermi energy of graphene approaches half the G-mode phonon energy [18–20], one might also expect significant anomalous G-mode softening, which could lead to a non-linear correlation between ω_{2D} and ω_G (Fig. 4c).

In our study, the highest n attained near device collapse is $\approx 6 \times 10^{11}$ cm^{-2}. Assuming a Fermi velocity $v_F = 1.3 \times 10^6$ m/s in suspended graphene [11, 12], this value corresponds to a Fermi energy shift close to $\hbar\omega_G/2$. As can be seen in Fig. 4d, the gate-induced G-mode softening is also accompanied by a reduction of Γ_G by ≈ 3 cm^{-1}. This line narrowing cannot be explained by tensile strain and is, however, expected due to a reduction of Landau damping in doped graphene [18, 19, 50, 51, 56]. Nevertheless, the smooth decrease of Γ_G with increasing n observed here contrasts with the "flat hat" behavior theoretically expected at 4 K, in the absence of charge inhomogeneity (see Fig. 4d). This discrepancy can be rationalized by considering a small residual charge inhomogeneity on the order of 5×10^{10} cm^{-1} [57]. In such conditions, the G-mode frequency is not expected to vary significantly with the gate-induced doping (see gray bar in Fig. 4c). We also note that the 2D-mode frequency is expected to be virtually independent of the doping level for $|n| < 10^{12}$ cm^{-2} [51, 56].

We thus conclude that the G- and 2D-mode softening are essentially due to electrostatically-induced tensile strain, with a possible minor contribution from anomalous G-mode softening that may lead to a linear correlation with a slope slightly smaller that typically reported values [29, 37, 38, 53–55]. Our results demonstrate that the elusive phonon anomalies [20] will be in-

trinsically challenging to unveil in monolayer graphene as their fingerprints will be smeared out by tiny residual charge inhomogeneity and strain-induced phonon softening. However, the impact of the charge carrier concentration can still be probed through the narrowing of the G-mode feature (see Fig. 4d). With the maximum G-mode frequency downshift of $\approx -5.5\,\mathrm{cm}^{-1}$ with respect to its initial value at $V_\mathrm{g} = 0$, we estimate an electrostatically-induced strain of $\sim 0.15\,(0.10)\,\%$ in the case of uniaxial (biaxial) stress [29, 34, 37, 53, 55, 58]. This *local* strain evaluated through phonon softening in the middle of the trench is in qualitative agreement with an estimated *average* strain of 0.3 ± 0.1 % based on the measurement of ξ and assuming a parabolic profile. These estimations suggest that the electrostatically-applied stress is predominantly uniaxial, as can be expected within our sample geometry (see Fig. 1a). The difference between the local and average strains indicates that strain near the edges of the trench is significantly larger than in the middle of the trench [16]. Near collapse, tensile strain may lead to a slight broadening of the G-mode feature ($\sim 1-2\ \mathrm{cm}^{-1}$) that may partly compensate the suppression of Landau damping at large gate bias (see Fig. 4d for $n \gtrsim 5\times10^{11}\ \mathrm{cm}^{-2}$).

Conclusion Using Raman spectroscopy, we have achieved a contactless, minimally invasive study of electrostatically-gated suspended graphene. The membrane deflection is estimated with a vertical resolution as low as a few nm and a diffraction-limited lateral resolution. A simple electromechanical model provides a faithful description of the membrane deflection, up to irreversible collapse, and an estimation of the built-in tension, a poorly controlled parameter, however of utmost importance in nanoresonators. Importantly, we precisely identify and separate the contributions of strain and doping in the Raman spectrum of suspended graphene. Accurate monitoring and control of the deflection, stain and doping in suspended graphene and related atomically-thin materials is appealing not only for device engineering but also for opto-(electro)mechanical investigations [7, 8, 59–63].

Acknowledgement We thank F. Federspiel, K. Makles, and P. Verlot for fruitful discussions, F. Chevrier, A. Boulard, M. Romeo, and F. Godel for experimental support, R. Bernard, S. Siegwald, and H. Majjad for assistance in the STNano clean room facility. We acknowledge financial support from C'Nano GE, the Agence Nationale de Recherche (ANR) under grants QuandDoGra 12 JS10-00101 and H2DH ANR-15-CE24-0016 and the University of Strasbourg Institute for Advanced Study (USIAS, GOLEM project).

[1] M. L. Ekinci, K. L. & Roukes, Rev. Sci. Instrum. **76**, 061101 (2005).
[2] V. Sazonova, Y. Yaish, H. Üstünel, D. Roundy, T. A. Arias, and P. L. McEuen, Nature **431**, 284 (2004).
[3] J. S. Bunch, A. M. van der Zande, S. S. Verbridge, I. W. Frank, D. M. Tanenbaum, J. M. Parpia, H. G. Craighead, and P. L. McEuen, Science **315**, 490 (2007).
[4] C. Chen, S. Rosenblatt, K. I. Bolotin, W. Kalb, P. Kim, I. Kymissis, H. L. Stormer, T. F. Heinz, and J. Hone, Nature Nano **4**, 861 (2009).
[5] J. Lee, Z. Wang, K. He, J. Shan, and P. X.-L. Feng, ACS Nano **7**, 6086 (2013).
[6] A. Castellanos-Gomez, R. van Leeuwen, M. Buscema, H. S. J. van der Zant, G. A. Steele, and W. J. Venstra, Adv. Mater. **25**, 6719 (2013).
[7] R. A. Barton, I. R. Storch, V. P. Adiga, R. Sakakibara, B. R. Cipriany, B. Ilic, S. P. Wang, P. Ong, P. L. McEuen, J. M. Parpia, and H. G. Craighead, Nano Lett. **12**, 4681 (2012).
[8] A. Reserbat-Plantey, L. Marty, O. Arcizet, N. Bendiab, and V. Bouchiat, Nature Nano **7**, 151 (2012).
[9] K. I. Bolotin, K. J. Sikes, Z. Jiang, M. Klima, G. Fudenberg, J. Hone, P. Kim, and H. L. Stormer, Solid State Commun. **146**, 351 (2008).
[10] X. Du, I. Skachko, A. Barker, and E. Y. Andrei, Nat Nano **3**, 491 (2008).
[11] D. C. Elias, R. V. Gorbachev, A. S. Mayorov, S. V. Morozov, A. A. Zhukov, P. Blake, L. A. Ponomarenko, I. V. Grigorieva, K. S. Novoselov, F. Guinea, and A. K. Geim, Nature Physics **7**, 701 (2011).
[12] C. Faugeras, S. Berciaud, P. Leszczynski, Y. Henni, K. Nogajewski, M. Orlita, T. Taniguchi, K. Watanabe, C. Forsythe, P. Kim, R. Jalil, A. Geim, D. Basko, and M. Potemski, Phys. Rev. Lett. **114**, 126804 (2015).
[13] M. Huang, T. A. Pascal, H. Kim, W. A. Goddard, and J. R. Greer, Nano Lett. **11**, 1241 (2011).
[14] H. Zhang, J.-W. Huang, J. Velasco Jr., K. Myhro, M. Maldonado, D. D. Tran, Z. Zhao, F. Wang, Y. Lee, G. Liu, W. Bao, and C. N. Lau, Carbon **69**, 336 (2014).
[15] M. V. Medvedyeva and Y. M. Blanter, Phys. Rev. B **83**, 045426 (2011).
[16] W. Bao, K. Myhro, Z. Zhao, Z. Chen, W. Jang, L. Jing, F. Miao, H. Zhang, C. Dames, and C. N. Lau, Nano Lett. **12**, 5470 (2012).
[17] L. D. Landau and E. M. Lifshitz, Theory of elasticity, 2nd ed., edited by P. P. Ltd., Vol. 7 (Pergamon Press, 1970).
[18] M. Lazzeri and F. Mauri, Phys. Rev. Lett. **97**, 266407 (2006).
[19] T. Ando, J. Phys. Soc. Jpn. **75**, 124701 (2006).
[20] J. Yan, E. A. Henriksen, P. Kim, and A. Pinczuk, Phys. Rev. Lett. **101**, 136804 (2008).
[21] D. M. Basko, Phys. Rev. B **78**, 125418 (2008).
[22] S. Berciaud, X. Li, H. Htoon, L. Brus, S. Doorn, and T. Heinz, Nano Lett. **13**, 3517 (2013).
[23] S. Berciaud, S. Ryu, L. E. Brus, and T. F. Heinz, Nano Lett. **9**, 346 (2009).
[24] A. C. Ferrari and D. M. Basko, Nature Nano **8**, 235 (2013).
[25] Z. H. Ni, T. Yu, Z. Q. Luo, Y. Y. Wang, L. Liu, C. P.

Wong, J. Miao, W. Huang, and Z. X. Shen, ACS Nano, ACS Nano **3**, 569 (2009).
[26] D. Metten, F. Federspiel, M. Romeo, and S. Berciaud, physica status solidi (b) **250**, 2681 (2013).
[27] D. Yoon, H. Moon, Y.-W. Son, J. S. Choi, B. H. Park, Y. H. Cha, Y. D. Kim, and H. Cheong, Phys. Rev. B **80**, 125422 (2009).
[28] A. Reserbat-Plantey, S. Klyatskaya, V. Reita, L. Marty, O. Arcizet, M. Ruben, N. Bendiab, and V. Bouchiat, Journal of Optics **15**, 114010 (2013).
[29] D. Metten, F. Federspiel, M. Romeo, and S. Berciaud, Phys. Rev. Applied **2**, 054008 (2014).
[30] W. Bao, F. Miao, Z. Chen, H. Zhang, W. Jang, C. Dames, and C. N. Lau, Nat Nano **4**, 562 (2009).
[31] D. Yoon, Y.-W. Son, and H. Cheong, Nano Lett. **11**, 3227 (2011).
[32] V. Singh, S. Sengupta, H. S. Solanki, R. Dhall, A. Allain, S. Dhara, P. Pant, and M. M. Deshmukh, Nanotechnology **21**, 165204 (2010).
[33] J. S. Bunch, S. S. Verbridge, J. S. Alden, A. M. van der Zande, J. M. Parpia, H. G. Craighead, and P. L. McEuen, Nano Lett. **8**, 2458 (2008).
[34] A. L. Kitt, Z. Qi, S. Rémi, H. S. Park, A. K. Swan, and B. B. Goldberg, Nano Lett. **13**, 2605 (2013).
[35] D. Metten, G. Froehlicher, and S. Berciaud, Phys. Status Solidi B **252**, 2390 (2015).
[36] In the range of gate biases applied here, I_{G} and I_{2D} are expected to vary marginally due to electrostatically-induced doping [51, 56].
[37] T. M. G. Mohiuddin, A. Lombardo, R. R. Nair, A. Bonetti, G. Savini, R. Jalil, N. Bonini, D. M. Basko, C. Galiotis, N. Marzari, K. S. Novoselov, A. K. Geim, and A. C. Ferrari, Phys. Rev. B **79**, 205433 (2009).
[38] M. Huang, H. Yan, C. Chen, D. Song, T. F. Heinz, and J. Hone, Proceedings of the National Academy of Sciences **106**, 7304 (2009).
[39] H. Hencky, Z. angew. Math. Phys. **63**, 311 (1915).
[40] U. Komaragiri, M. R. Begley, and J. G. Simmonds, Journal of Applied Mechanics **72**, 203 (2005).
[41] K. Yue, W. Gao, R. Huang, and K. M. Liechti, Journal of Applied Physics **112**, 083512 (2012).
[42] J. J. Vlassak and W. D. Nix, Journal of Materials Research **7**, 3242 (1992).
[43] J. W. Beams, In structures and properties of thin films, edited by C. A. Neugebauer (Wiley, New York, 1995).
[44] J. G. Williams, Int. Journal of Fracture **87**, 265 (1997).
[45] G. E. Bacon, Acta Cryst. **4**, 558 (1951).
[46] C. Lee, X. Wei, J. W. Kysar, and J. Hone, Science **321**, 385 (2008).
[47] J.-W. Jiang, J.-S. Wang, and B. Li, Phys. Rev. B **80**, 113405 (2009).
[48] S. P. Koenig, N. G. Boddeti, M. L. Dunn, and J. S. Bunch, Nat Nano **6**, 543 (2011).
[49] R. J. T. Nicholl, H. J. Conley, N. V. Lavrik, I. Vlassiouk, Y. S. Puzyrev, V. P. Sreenivas, S. T. Pantelides, and K. I. Bolotin, Nature Communications **6**, 8789 (2015).
[50] S. Pisana, M. Lazzeri, C. Casiraghi, K. S. Novoselov, A. K. Geim, A. C. Ferrari, and F. Mauri, Nat. Mater. **6**, 198 (2007).
[51] G. Froehlicher and S. Berciaud, Phys. Rev. B **91**, 205413 (2015).
[52] N. Bonini, M. Lazzeri, N. Marzari, and F. Mauri, Phys. Rev. Lett. **99**, 176802 (2007).
[53] J. Zabel, R. R. Nair, A. Ott, T. Georgiou, A. K. Geim, K. S. Novoselov, and C. Casiraghi, Nano Lett. **12**, 617 (2011).
[54] J. E. Lee, G. Ahn, J. Shim, Y. S. Lee, and S. Ryu, Nature Communications **3**, 1024 (2012).
[55] C. Androulidakis, E. N. Koukaras, J. Parthenios, G. Kalosakas, K. Papagelis, and C. Galiotis, Scientific reports **5**, 18219 (2015).
[56] J. Yan, Y. Zhang, P. Kim, and A. Pinczuk, Phys. Rev. Lett. **98**, 166802 (2007).
[57] Let us note that laser-induced heating is unlikely to play a role since we find very similar variations of ω_{G} and Γ_{G} due to electron-phonon coupling at 4 K and 100 K (see Fig. 4c), a temperature that is well above the unavoidable laser heating we can estimate in our conditions.
[58] I. Polyzos, M. Bianchi, L. Rizzi, E. N. Koukaras, J. Parthenios, K. Papagelis, R. Sordan, and C. Galiotis, Nanoscale **7**, 13033 (2015).
[59] A. Reserbat-Plantey, K. G. Schädler, L. Gaudreau, G. Navickaite, J. Güttinger, D. Chang, C. Toninelli, A. Bachtold, and F. H. Koppens, Nature communications **7** (2016).
[60] D. Davidovikj, J. J. Slim, S. J. Cartamil-Bueno, H. S. J. van der Zant, P. G. Steeneken, and W. J. Venstra, Nano Letters **16**, 2768 (2016).
[61] R. D. Alba, F. Massel, I. R. Storch, T. S. Abhilash, A. Hui, P. L. McEuen, H. G. Craighead, and J. M. Parpia, Nature Nanotechnology **advance online publication** (2016), 10.1038/nnano.2016.86.
[62] J. P. Mathew, R. N. Patel, A. Borah, R. Vijay, and M. M. Deshmukh, Nature Nanotechnology **advance online publication** (2016), 10.1038/nnano.2016.94.
[63] C. Schwarz, B. Pigeau, L. M. de Lépinay, A. Kuhn, D. Kalita, N. Bendiab, L. Marty, V. Bouchiat, and O. Arcizet, arXiv preprint arXiv:1601.00154 (2016).
[64] J.-U. Lee, D. Yoon, and H. Cheong, Nano Lett. **12**, 4444 (2012).
[65] Z. Luo, C. Cong, J. Zhang, Q. Xiong, and T. Yu, Applied Physics Letters **100**, 243107 (2012).
[66] P. Venezuela, M. Lazzeri, and F. Mauri, Phys. Rev. B **84**, 035433 (2011).
[67] A. Das, S. Pisana, B. Chakraborty, S. Piscanec, S. K. Saha, U. V. Waghmare, K. S. Novoselov, H. R. Krishnamurthy, A. K. Geim, A. C. Ferrari, and A. K. Sood, Nat Nano **3**, 210 (2008).
[68] P. Blake, E. W. Hill, A. H. Castro Neto, K. S. Novoselov, D. Jiang, R. Yang, T. J. Booth, and A. K. Geim, Appl. Phys. Lett. **91**, 063124 (2007).

Supporting Information

SI 1. FITTING PROCEDURES

The G-mode feature is fit to a Lorentzian profile and its spectral position ω_G, FWHM Γ_G and integrated intensity I_G are extracted. The 2D-mode feature shows a slight asymmetry, as often observed on clean suspended graphene devices [22, 23, 64, 65]. Here, following Refs. [21, 22, 66], we phenomenologically use the sum of two Lorentzian profiles at the power 3/2 with a shared FWHM in order to fit the 2D-mode feature and identify two subfeatures located at ω_{2D_-} and ω_{2D_+}. The low-energy feature is more intense (here, I_{2D_-}/I_{2D_+} is 2.5 ± 0.3) and $\omega_{2D_+} - \omega_{2D_-}$ is constantly $(12 \pm 0.5)\,\mathrm{cm}^{-1}$). In this Letter, we use ω_{2D_-} to define the 2D-mode frequency ω_{2D}.

SI 2. RAMAN CHARACTERIZATION AT ROOM TEMPERATURE

Before our low-temperature study, the suspended graphene device has been characterized at room temperature by means of Raman spectroscopy using a laser beam at 532 nm. The G- and 2D-mode features are fit with the above-described procedure. The frequencies ω_G, ω_{2D} and the linewidth Γ_G are extracted. Figures S1a and b show Raman maps of ω_G and Γ_G.

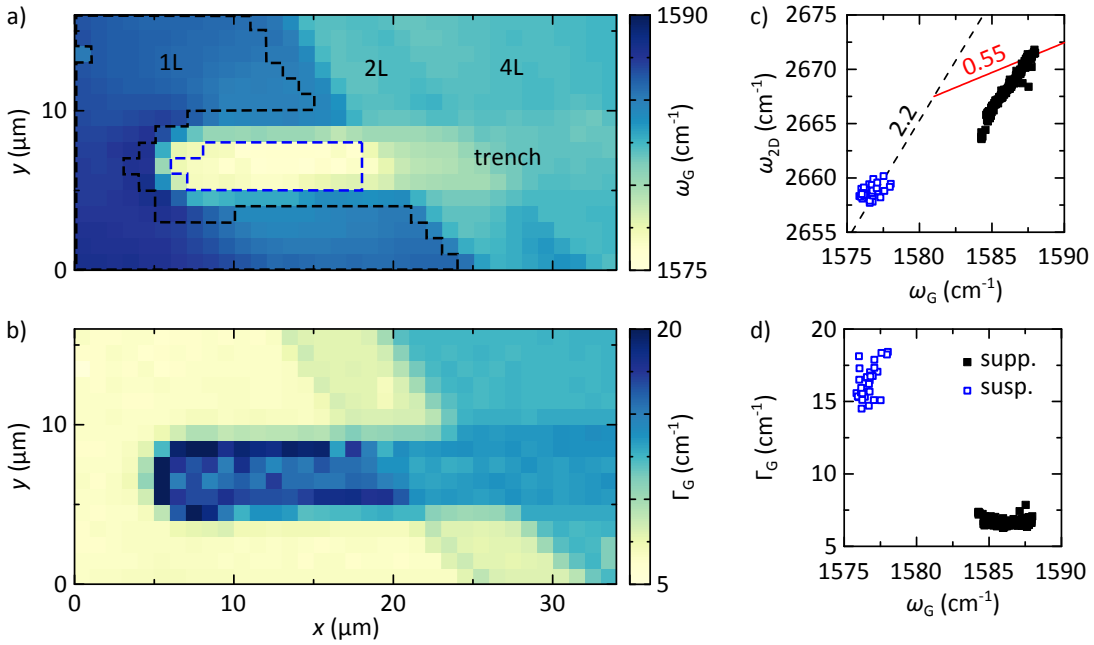

FIG. S1. (a) and (b) Room temperature hyperspectral Raman maps of the device, with a step size of 1 μm, showing the distribution of ω_G and Γ_G, respectively. The data taken into account for further analysis in (c) and (d) are delimited by a black (blue) dashed line in (a), for the supported (suspended) area. The suspended area is well distinguishable and characterized by a relatively low ω_G and high Γ_G. (c) Correlation of ω_G and ω_{2D} using the data extracted from the maps in (a) and (b). Data of the suspended (supported) area [see dashed lines in (a)] are shown as open blue (filled black) squares. A slope of $\partial\omega_{2D}/\partial\omega_G = 2.2$ for strain [29, 53, 54] and 0.55 for hole doping [51, 67] are added as dashed black and straight red lines, respectively.

The graphs in Fig. S1c and d correlate ω_G with ω_{2D} and Γ_G, respectively. The data are extracted from the delimited areas on the map in Fig. S1a and plotted as open blue squares for the suspended area and filled black

squares for the supported area. On Fig. S1c the data are concentrated with a small standard deviation and line up along a slope of 2.2. Here we use the reference point ($\omega_{\mathrm{G}}^0 = 1581\,\mathrm{cm}^{-1}$, $\omega_{\mathrm{2D}}^0 = 2667\,\mathrm{cm}^{-1}$), as in ref. [26] for neutral, unstrained suspended graphene at 300 K and for a laser wavelength of 532 nm. In contrast, the data of the supported area are aligned along a line with the same slope of 2.2 but shifted to a higher ω_{G} due to substrate-induced doping. Following the vector decomposition model proposed by Lee *et al.* [54] and applied to our suspended sample, we might estimate an average tensile strain of $0.06 \pm 0.01\,\%$ and a doping level $\lesssim 10^{11}\,\mathrm{cm}^{-2}$. The latter is in stark contrast with the doping level of the supported part, which is of one order of magnitude larger. The data represented in Fig. S1d combine the two maps in Fig. S1a and b, and confirm the quasi-undoped character of the membrane by the two well-distinguishable areas in the ω_{G}-Γ_{G}-plane [18, 23].

SI 3. RAMAN ENHANCEMENT DUE TO OPTICAL INTERFERENCES

The trench on which graphene is exfoliated and suspended can be considered as a multilayered system, *i.e.* [Si - SiO_2 - air/vacuum - graphene - air/vacuum]. The involved layer thicknesses are on the same order of magnitude as the wavelength of the light, so that optical interference effects come into play. We model the evolution of the ratio of the incoming and scattered electrical field with a Fabry-Pérot calculation, according to

$$A_{j+1,j} = \frac{r_{j+1,j} + A_{j,j-1}e^{2i\phi_j}}{1 + r_{j+1,j}A_{j,j-1}e^{2i\phi_j}}. \tag{S1}$$

Here, r_{ij} are the reflection coefficients at the i/j interface and the phase is defined as $\phi_i = 2\pi\tilde{n}_i d_i/\lambda$. The Raman interaction takes place in the last (graphene) layer and has to be considered separately. Multiple reflections within the graphene layer for the incoming (laser) and Raman-scattered light are calculated by taking the effective reflection coefficient (on one side of the graphene membrane). An optical enhancement factor is then obtained by integrating over the thickness t of the membrane [27, 68] according to

$$\text{Enhancement factor} = \int_0^t \left| \frac{E_x}{E_0} \times \frac{E_{\mathrm{out}}}{E_R} \right|^2 \mathrm{d}x, \tag{S2}$$

where E_0 is the electric field of the incoming laser beam, E_x the electric field of the incoming laser beam at the position x where the Raman interaction takes place, E_{R} the Raman electric field created at x and E_{out} the Raman electric field coming out of the layered system. The enhancement factor is generally normalized relative to the case of monolayer graphene in free space. Here, for a clearer comparison with our experimental data (see Fig. 2a and 2b in the main text), we renormalize the amplitude of the enhancement factor variations (between its minimal and maximal values) by the measured ratio between the minimal and maximal integrated Raman intensities we have observed experimentally. This renormalization has no significant consequence on the determination of the membrane deflection.

SI 4. DETAILS ON THE ELECTROMECHANICAL MODEL

The deflection is modeled by regarding the electrostatic pressure on the membrane, which writes

$$p_{\mathrm{el}}\left(V_{\mathrm{g}}, \xi(x)\right) = \frac{\varepsilon_0 \varepsilon_{\mathrm{SiO_2}}^2 V_{\mathrm{g}}^2}{2\left(h_{\mathrm{SiO_2}} + \varepsilon_{\mathrm{SiO_2}}(h_0 - \xi(x))\right)^2}. \tag{S3}$$

$\xi(x)$ is the deflection profile perpendicular to the trench (x direction), ε_0 the dielectric constant, $\varepsilon_{\mathrm{SiO_2}}$ the relative dielectric constant of SiO_2 and $h_{\mathrm{SiO_2}}$ the residual oxide thickness.

The membrane deflection in the middle of the trench (simply denoted ξ in the main manuscript), induced by a uniform pressure load writes [15, 16]

$$p_{\mathrm{el}}(\xi) = \frac{64Et}{3(1-\nu^2)L^4}\,\xi^3 + \frac{8T_0}{L^2}\,\xi, \tag{S4}$$

where E is the Young's modulus, ν the Poisson ratio and t the thickness of the membrane, L the width of the trench (see Fig. 1b in the main text) and T_0 its pre-strain (in N/m). As mentioned in the main text, the scaling

$p_{\mathrm{el}} \propto \xi^3$ is well-known for membranes (without bending rigidity) [29, 39–41], and the additional pre-strain-term can be interpreted as an effective bending rigidity moderating the deflection, as p_{el} scales linearly with ξ for thin plates [15, 17, 42–44].

Eq. (S4) is obtained from the equation of equilibrium [17],

$$p_{\mathrm{el}}(\xi(x)) = D\,\frac{\partial^4 \xi(x)}{\partial x^4} - T(\xi'(x))\,\frac{\partial^2 \xi(x)}{\partial x^2}, \tag{S5}$$

by supposing a parabolic profile of the membrane, and where $T = T_{\mathrm{e}} + T_0$ is the total strain in the membrane, with T_{e} the strain due to the electrostatically induced deflection. The profile is taken as $\xi(x) = p_{\mathrm{el}}(L^2/4 - x^2)/(2T)$, which is a first approximation, because back coupling mechanisms between the deflection and the charge redistribution within the membrane are neglected. However, Eq. (S5) can be self-consistently solved considering a parabolic profile.

As discussed in the main text, Eq. (S4) requires a uniform pressure load over the membrane, which is calculated as an average value of p_{el}, obtained by integrating the local capacitance c along the parabolic profile $\xi(x)$:

$$p_{\mathrm{el}}(\xi) = \frac{V_{\mathrm{g}}^2}{2\varepsilon_0} \int_{-L/2}^{+L/2} c^2\,(x)\ \frac{\mathrm{d}x}{L}, \tag{S6}$$

with $c(x) = (c_0^{-1}(x) + c_{\mathrm{SiO_2}}^{-1})^{-1}$, $c_{\mathrm{SiO_2}} = \varepsilon_0 \varepsilon_{\mathrm{SiO_2}}/(h_{\mathrm{SiO_2}})$ and $c_0(x) = \varepsilon_0/(h_0 - \xi(x))$ the distance between the SiO_2 layer and the membrane, ε_0 is the vacuum permittivity and $\epsilon_{\mathrm{SiO_2}} \approx 3.9$ is the DC dielectric constant of SiO_2. We can thus compute ξ as a function of V_{g} by injecting Eq. (S6) into Eq. (S4):

$$V_{\mathrm{g}}^2 = \frac{\frac{4\varepsilon_0}{c_{\mathrm{SiO_2}}^2}\left(\frac{8T_0}{L^2}\ \xi + \frac{64Et}{3(1-\nu^2)L^4}\ \xi^3\right)}{\sqrt{\frac{\varepsilon_0}{B^3 c_{\mathrm{SiO_2}}\xi}}\ \arctan\left(\sqrt{\frac{c_{\mathrm{SiO_2}}\xi}{\varepsilon_0 B}}\right) + \frac{1}{B^2 + \frac{c_{\mathrm{SiO_2}}\xi}{\varepsilon_0}B}}. \tag{S7}$$

Here, $B = 1 + c_{\mathrm{SiO_2}}\ (h_0 - \xi)\,/\varepsilon_0$ and the pre-strain T_0 can be used as a fitting parameter, as shown in Fig. 3a in the main text. Equation S7 is solved numerically.

SI 5. DEFLECTION EXTRACTED FROM I_{2D}

The values of ξ presented in Fig 3a of the main manuscript are derived from the integrated intensity of the G-mode feature I_G. In Fig. S2 we show the data extracted from I_{2D} and the corresponding fit using our electromechanical model. A pre-strain of $T_0 = 0.28\,\mathrm{N/m}$ is found, which is comparable the one extracted from I_G.

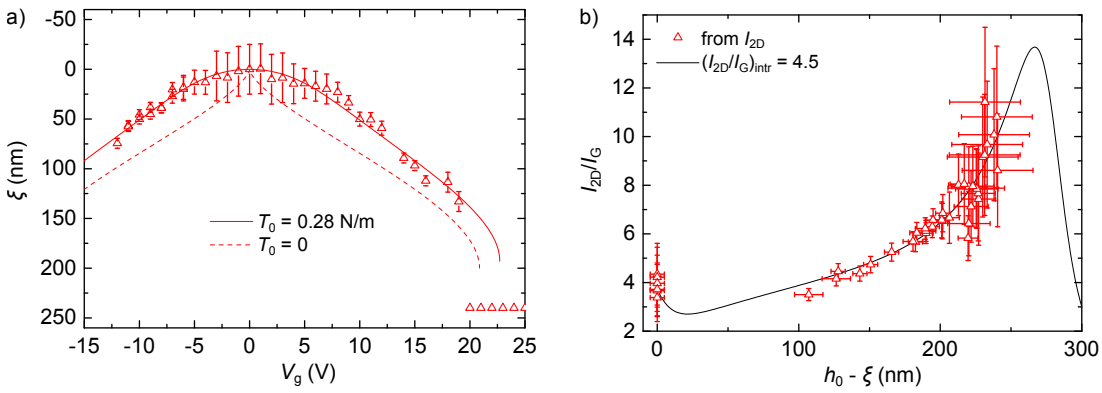

FIG. S2. Vertical deflection ξ in the middle of the trench, determined by the variation of I_{2D}, as a function of V_g. The dashed red line is the electromechnical model with $T_0 = 0$ whereas the solid line is with T_0 as fitting parameter ($T_0 = 0.28\,\mathrm{N/m}$). (b) Evolution of I_{2D}/I_G as a function of $h_0 - \xi$, determined from the evolution of I_{2D} with V_g. The red line is a fit based on a multiple interference model using an *interference-free* reference value of $(I_{2D}/I_G)_{intr} = 4.5$, much similar to the value proposed in the main text (see also Fig. 2c).

SI 6. ELECTROMECHANICAL CALCULATIONS FOR VARIOUS SiO_2 THICKNESS

Commonly used Si/SiO_2 substrates have oxide thickness of 285 and 90 nm. In Fig. S3, we show data similar to Fig. 3b-c in the main manuscript for for $L = 5\,\mu$m and $L = 3\,\mu$m, respectively.

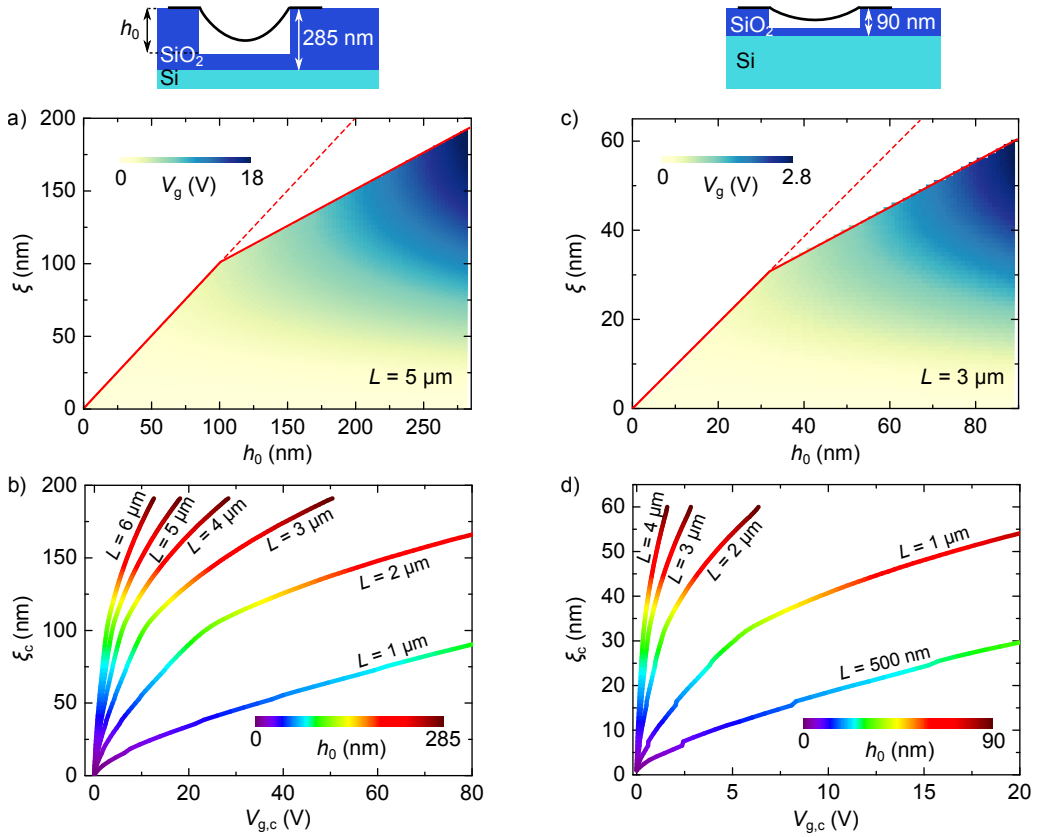

FIG. S3. (a) False color map of the gate voltage required to attain a given ξ as a function of h_0, for $L = 5\,\mu$m and an initial SiO_2 thickness of 285 nm [see schematic above (a)]. (b) Critical deflection ξ_c as a function of the corresponding critical gate voltage $V_{g,c}$. The data are extracted from the color plots, as explained in the main text. The critical lines are shown for different trench widths L. The color code indicates the corresponding h_0. (c) False color map as in (a), plotted for an initial SiO_2 thickness of 90 nm and a trench width of $L = 3\,\mu$m. (d) As in (b), the critical deflection ξ_c is plotted as a function of $V_{g,c}$ and h_0. The chosen values of L are adapted to the smaller values of h_0.

SI 7. CRITICAL CHARGE CARRIER DENSITY

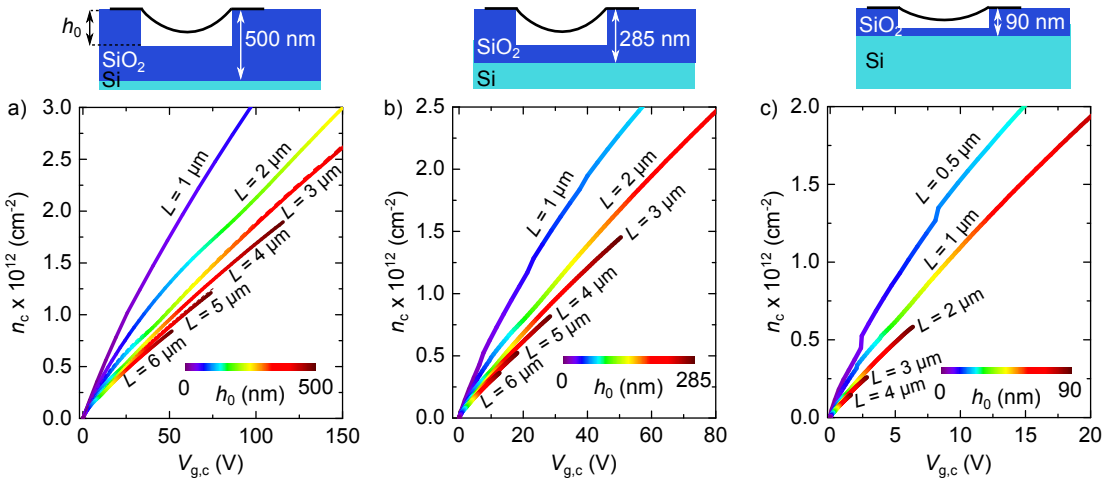

FIG. S4. The charge carrier density in the middle of the trench is calculated according to $n(V_g, \xi) = \frac{\varepsilon_0 \varepsilon_{SiO_2} V_g}{\varepsilon_{SiO_2}(h_0 - \xi) + h_{SiO_2}}$. In (a), (b) and (c) the predicted critical charge carrier density n_c as a function of the critical gate voltage (near membrane collapse) and h_0 are shown for an initial oxide thickness of 500, 285 and 90 nm.

SI 8. SCANNING ELECTRON MICROSCOPY (SEM) IMAGING

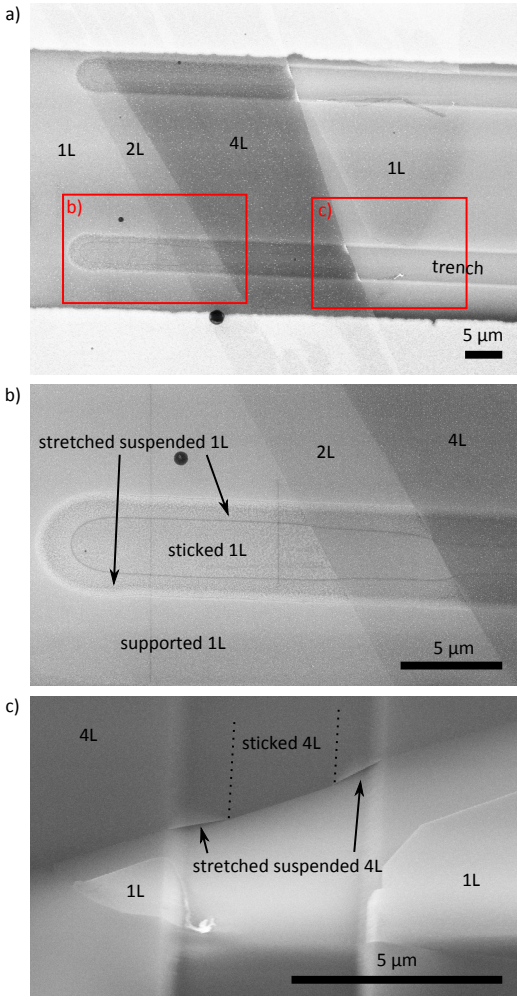

FIG. S5. SEM images of the device after the gate-dependent Raman study, after the membrane has collapsed and adheres to the bottom of the trench. (a) Overview of the device with red squares indicating the zoomed area in (b) and (c). (b) The collapsed area can be distinguished by a light gray line in the bottom. Also the neighboring 2LG and 4LG are stuck to the substrate. The stretched suspended part at the borders of the trench is seen in (c) for the 4LG, where the image is rotated by 90 degrees and slightly tilted. The scale bar is 5 μm in all images.